RESEARCH PAPER

Fatigue and Progressive Damage of Thin Woven CFRP Plates Weakened by Circular Holes

L. Heinzlmeier[1,2] · S. Sieberer[1] · C. Kralovec[1] · M. Schagerl[1,2]

Abstract

Background In order to design thin-walled components it is necessary to consider the presence of holes and their effects. For high performance composite structures, this is still an issue, since usually only coupons are used in experimental observations and the influence of free edges and the hole affects the fatigue behavior mutually.

Objective This work aims to find, through experimental trials, an empirical model that can be used to describe and predict the damage propagation, originating from a circular hole.

Methods A fatigue test series is performed and the damage initiation and propagation is monitored with three-dimensional digital image correlation, with which the occurring damage can be measured. Validation of the experimentally induced damage size measured with digital image correlation is performed intermediate with an *in-situ* measurement with active thermography and phased array ultrasonic. The novelty of this approach is that wide specimens are used, where the influence of the free edges on the hole does not occur.

Results The progression of the detected damage over the test reflects the applied loads, where higher loads cause larger damage. For all defined load levels a similar damage propagation is identified, allowing to establish an empirical model and fit it to the test data.

Conclusion The proposed empirical model provides a novel approach to describe and predict damage propagation originating from a circular hole in thin-walled composite plates. In addition, it is shown that the damage propagation ceases for the selected plate configuration and thus does not lead to a complete failure.

Keywords CFRP · Plate with hole · Plain-woven composites · Tension-tension loading · Fatigue · Digital image correlation

Introduction

In order to achieve the climate targets set by the International Civil Aviation Organization (ICAO), the Carbon Offsetting and Reduction Scheme for International Aviation (CORSIA) has been defined as a roadmap for civil aviation to fulfill its part in lowering emissions. A voluntary pilot phase began in January 2021. Primarily, this regulation affects the airlines. Thus, aircraft manufacturers are also responding to this scheme and developing more fuel-efficient aircrafts [1, 2]. One option for aircraft manufacturers, which is already applied, is to use advanced materials, such as carbon fiber-reinforced plastics (CFRP). CFRP have been used increasingly in commercial aviation for the last 40 years and nowadays, these advanced composite materials account for up to 50% of the mass of modern aircrafts. In future, the growth is expected to continue [3, 4].

During assembly, the individual parts have to be connected together. To join the components, usually holes are machined, in which bolts or rivets are inserted. The holes are causing stress concentrations, which can significantly reduce the strength and may lead to premature failure of the structure. Consequently, it is crucial to assess the stress state surrounding holes. Lekhnitskii et al. [5] and Savin [6] were concerned with the analytical description of stresses around cutouts (e.g. holes) in anisotropic and orthotropic plates.

✉ L. Heinzlmeier
  lukas.heinzlmeier@jku.at

1 Institute of Structural Lightweight Design, Johannes Kepler University Linz, Altenberger Straße 69, Linz 4040, Upper Austria, Austria

2 Christian Doppler Laboratory for Structural Strength Control of Lightweight Constructions, Johannes Kepler University Linz, Altenberger Straße 69, Linz 4040, Upper Austria, Austria

They introduced complex stress variables with which the boundary value problems could be solved. Based on their formulations, new approaches to determine the stresses around holes under static loading have been derived. Frequently used approaches were developed by Whitney and Nuismer [7]. They proposed the average stress criterion and the point stress criterion. For both, the stress in the loading direction is compared to the tensile strength of the same plate without a hole. In the case that the stress in loading direction is equal to the tensile strength, damage will occur. The average stress criterion averages the stress in the vicinity of the hole over a small area. Whereas the point stress criterion evaluates the stress at a single point in the vicinity of the hole. Karlak [8] reported, that the assumptions made in that context are not generally valid and require modification.

However, if the loading is cyclic, the damage behavior for plates with a circular hole becomes more complex. Depending on the laminate design, the size and location of the hole, the material constituents and the applied load, different damage modes can be activated. In general, the damage under cyclic loading is a combination of matrix cracks, fiber breakage, delaminations and debonding between fiber and matrix. According to Aymerich and Found [9], and Ambu et al. [10], the damage caused by cyclic tensile loading leads to a reduction in the stress concentration. This means that the load carrying capacity compared to the initial load carrying capacity is increased. Nevertheless, the growth of the damage proceeds, until final failure occurs. In their investigations, only narrow specimens made from UD plies were taken into account, whereas in aeronautical applications, woven fabrics are often preferred due to their superior impact resistance.

To fully understand the effect of a hole on structural components under cyclic loading, experimental investigations are required. Usually Open-Hole fatigue (OHF) standard testing is carried out, where narrow coupons are mainly used [11–13]. These show a short time of damage propagation after initiation in which the free edge and the hole mutually affect each other. Typical lightweight structures are plates and shells and thus, show a different damage propagation behavior after imitation. Consequently, larger structural elements, like plates, need to be considered for the investigation of the strength of mechanical components from damage initiation till failure.

In order to assess the initiation and propagation of damage, a number of methods are available, which have been established in recent years. Exemplarily, digital image correlation (DIC), ultrasonic flaw detection, x-ray methods and thermography are named. In the literature, several methods are usually applied together so that a validation is possible [10, 14–17]. Pirinu et al. investigated the fatigue behavior of holed CFRP elements under tensile and bending loads and utilized a DIC system along with active thermography and ultrasonic to determine damage.

However, coupons with small dimensions built up from unidirectional plies were used [18].

The objective of the present paper is to investigate the fatigue behavior of thin plain-woven CFRP plates with a circular hole, composed as an aircraft laminate [19], under cyclic tension-tension loading. In detail, the focus of the experimental investigation is placed on the damage initiation and propagation under different load levels. For this purpose, a three-dimensional digital image correlation system (3D-DIC) is used with which the damage is quantified by determining the area of damage. A validation of the determined area of damage is performed by using active thermography (AT) and phased array ultrasonic flaw detection (UFD). This work aims to find an empirical model with which the area of damage can be described as a function of the number of cycles. The article is structured as follows. First, the experimental procedure is presented, including the manufacturing procedure of the plates, the testing routine, the damage monitoring and the data evaluation. Subsequently, the experimental results and the validation of the measured damage are given. Following this, an empirical model is established with which the damage propagation in plates with an circular hole can be described. The final Section of this paper gives a Discussion of the results, along with Conclusions.

Experimental Procedure

The manufacturing procedure of the plates, which includes the specimen preparation, along with the description of the testing routine is explained in this Section. In addition, the explanation of the used measurement equipment, as well as the data evaluation is described.

Manufacturing Procedure

A single ply is composed of epoxy resin and carbon fiber tows of type Solvay CYCOM® 970 and 3k-T650, respectively. The plates are composed from four of these plain-woven prepreg plies. The plies are arranged $[0f/45f]_s$, which is used as an aircraft laminate, vacuum bagged and cured in an autoclave (120 °C, 0.9 MPa). The laminate thickness after curing is 0.816 mm with a fiber volume fraction of 0.6. The circular hole and the outer contour of the individual plates are cut by water jet cutting, as this manufacturing method has negligible influence on the fatigue behavior [20]. Hereafter, the holes and outer contours are finished by sanding and polishing Subsequent inspections of the individual plates to check if there are any damages caused by the hole cutting and finishing process are carried out using UFD and AT. Exemplary the result of an UFD (C-Scan) and AT measurement of a plate are given in Fig. 1. The identical
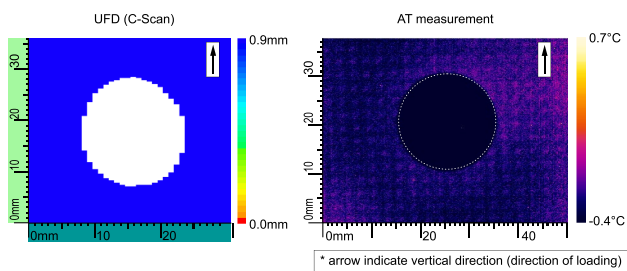
Fig. 1 Examination of the hole of a pristine plate to identify possible damage using UFD (C-Scan) and AT

parameters as listed in Tables 3 and 4 are used. However, the UFD measurements are carried out in a water basin. Each plate revealed that there was no induced damage and therefore all plates are used for the experimental investigations. After the inspection glass fiber-reinforced plastic (GFRP) tabs are applied to both ends of the plates, so that clamping in the test rig is possible. The tabs are bonded to the plates with a 2-component epoxy adhesive and cured at a temperature of 60 °C. To avoid dislocation of the tabs during the curing process, an in-house designed bonding device is used. Moreover, this device is used to apply a constant pressure to ensure an uniform bond layer thickness. In a final step, the close-up regions surrounding the holes (100 mm × 100 mm) are prepared for the 3D-DIC acquisition. For this purpose, a white primer is applied to create a base on which a fine, black speckle pattern is airbrushed. In Fig. 2, a representation of the tested plate with hole is illustrated, including the dimensions and GFRP tabs. Additionally, the close-up region covered with a speckle pattern is indicated.

Testing Routine

The testing procedure and experimental setup is the same for all plates. Only the chosen load during cyclic loading differs. All plates are subjected to cyclic tensile loading with a load ratio R = 0.1 and at a frequency of 4 Hz.

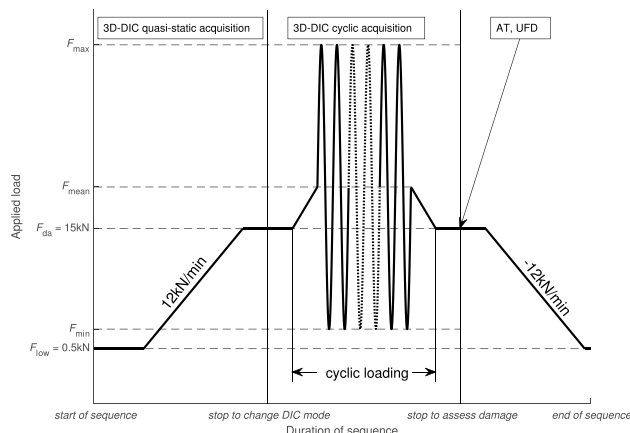The loads are applied with a servo-hydraulic cylinder with a nominal force of 100 kN. To control the servo-hydraulic
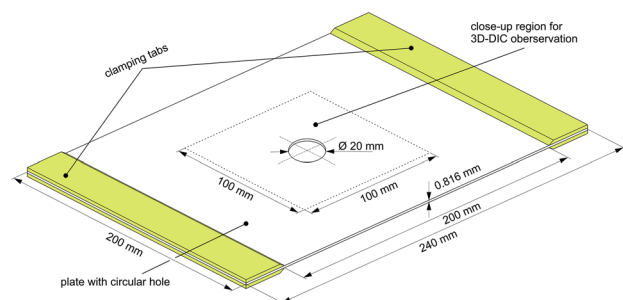
cylinder, a CUBUS controller from Zwick Roell® is used, with which the testing routine is executed. The testing routine contains a series of test sequences that are repeated multiple times. Each test sequence includes a quasi-static loading, a cyclic loading and a quasi-static unloading. A schematic representation of a single test sequence is depicted in Fig. 3. Additionally, the stops at which the measurements are carried out are indicated.

During quasi-static loading, the load is increased from the unloaded level F_{low} to the measuring level F_{da}. Before the cyclic loading between F_{max} and F_{min} is commenced, a pause is placed in which the acquisition mode of the 3D-DIC is changed from quasi-static acquisition to cyclic acquisition. This two acquisition modes are described in depth in "Digital Image Correlation (3D-DIC)" section. Once the desired amount of cycles has been reached, the load is returned to the measuring level F_{da}. Again the test sequence is paused and the damage is assessed by means of AT and UFD. After performing the measurements, the sequence is continued with a quasi-static unloading to the unloaded level F_{low}. Depending on the 3D-DIC measured area of damage, the number of cycles for the succeeding test sequences are determined. The single plates are tested until one of the chosen two stop criteria is reached. These are total failure or exceeding 2 million cycles.

In Fig. 4, the experimental setup and the placement of the used measurement equipment is given. The fundamental components, including the load cell, guiding bars and the in-house designed clamping device as well as a plate with hole, are shown. The foremost guiding bar and one leg of the 3D-DIC tripod are partially hidden for an improved visualisation.

The in-house designed clamping device consists of a base and an upper part. While the base part is fixed to the test rig, the upper part is mounted on the servo-hydraulic cylinder, with the load cell positioned in between. To

Fig. 2 Geometry and dimensions of the tested plate, location of the GFRP tabs and close-up region for the 3D-DIC acquisition

Fig. 3 Schematic representation of a test sequence, including the static and cyclic load domains and the stops, at which the measurements are carried out
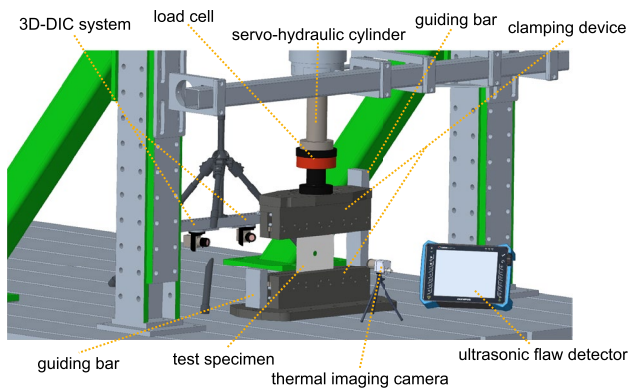
Fig. 4 Schematic visualization of the experimental setup and the arrangement of the used measurement equipment

Table 1 Specified load levels for the individual plates with load ratio R = 0.1

Plate number	Load level %	Peak load F_{max} [kN]	Trough load F_{min} [kN]
all	70	24.21	2.42
1	70	24.21	2.42
2	70	24.21	2.42
3	80	27.67	2.77
4	80	27.67	2.77
5	80	27.67	2.77
6	90	31.12	3.11
7	100	34.58	3.46
8	100	34.58	3.46
9	110	38.04	3.80

ensure that the upper part of the clamping device does not rotate about the cylinder axis, two guiding bars are used. The clamping jaws of the device are pressed together by bolts, thus creating the required clamping force to hold the plates in place. To counteract any reduction in clamping force by setting-in of tabs, an initial value of 20k cycles (k denotes thousand) at low load (70% of theoretical ultimate load) are defined. The bolts of the clamping jaws are tightened after 10k and 20k cycles. In addition, after these initial cycles, the first stops are made, in which the measuring of potential damage is performed. To exclude any issues of reclamping, the measurements are carried out on the mounted plate, while the measuring load F_{da} is acting.

Succeeding this initial cyclic loading the load is increased to the test load level.

Determination of the individual load levels is performed by the following procedure. Based on ASTM D4762-18 [21], the ultimate load for a 40 mm wide coupon without a hole, made from the same material, is determined. In accordance to the laminate theory, the load is scaled linearly with the width of the specimen, giving the ultimate load for the plate without a hole. For the quasi-isotropic plate, the stress concentration factor K_t is now considered. Assuming a stress concentration factor of $K_t = 3$, the theoretical ultimate load is equal to $F_{stat, max} = 34.58$ kN. This value is defined as 100% of the loading level in the present study. The specified loads for the individual plates are shown in Table 1. Also listed is the initial loading, that is defined as 70% of the theoretical ultimate load.

Damage Monitoring

This Subsection describes the measurement equipment and its application for damage initiation and propagation monitoring during mechanical testing of the considered plate with

hole. Furthermore, fundamentals of the applied measurement principles and defined measurement parameters are presented. Graphically, the arrangement of the measurement equipment is illustrated in Fig. 4.

Damage measurement application

To detect the initiation, and the damage propagation during cyclic loading, a 3D-DIC system from Correlated Solutions is used. This system is directed facing the close-up region surrounding the hole with the speckle pattern. Next to the 3D-DIC an external lamp is placed to provide a constant illumination over the length of the test. The force signal emitted by the CUBUS controller is transferred to the 3D-DIC and is used as a trigger signal.

Besides these 3D-DIC measurements, periodically non-destructive testing (NDT) methods are applied, as they are used to validate the threshold value for the 3D-DIC damage assessment.

As stated before, the NDT methods are carried out *in-situ* while the measuring load $F_{da} = 15$ kN is applied. In this process the measurements are performed each time after a cyclic loading block is completed. To minimize the influence on the speckle pattern and consequently falsify the 3D-DIC results, the NDT methods are executed on the plate face opposite to the 3D-DIC-observed one.

A MICRO-EPSILON® thermal imaging camera, of type TIM 450, and an external flash light are used to measure the damage size via AT. Following this method UFD is carried out. Therefore an Olympus Omniscan MX2 instrument and a phased array transducer is used. Water from a spray bottle is applied as coupling agent. The measurements are carried out by hand by pressing the transducer on the plate and moving it upwards in a continuous motion. Permanent spraying ensures that the signal is coupled in.

Digital Image Correlation (3D-DIC)

In order to obtain detailed information of displacements in experimental tests, digital image correlation is an established measuring method [10, 22]. Here, a large area can be covered and evaluated contact-free. If two cameras are used simultaneously, three-dimensional information of displacements can be obtained. The requirements for image correlation are the so-called features, which must be clearly assignable. If such features exist, their changes can be detected and tracked. The features can also be generated artificially by means of applied point clouds, the so-called speckle pattern. A variety of factors can lead to change the features. Exemplarily, mechanical loads and the resulting displacements, changes in illumination, or changes in camera settings, as well as damage to the features are mentioned [23]. To be able to capture such influences qualitatively, the used 3D-DIC system returns a quantity called sigma, which represents the first standard deviation confidence in the match (in pixels). A value of zero represents a perfect match, while a higher value of sigma indicates a low correlation quality. This means that the features cannot be detected clearly, or not at all [24]. If the environmental influences on the correlation can be avoided, then sigma can be interpreted as an indicator of damage. This approach has been applied already by Navarro et al. [22], in which damage propagation after impacts has been studied. Similarly, Sieberer et al. used 3D-DIC to detect damage initiation and damage propagation in discontinuous structural components [25, 26].

For the performed experimental tests, a 3D-DIC is used to acquire data obtained under quasi-static and cyclic loading, as compared to a 2D-DIC system, which requires only a single camera, the 3D-DIC system has the advantage that it can detect out-of-plane changes, such as potential appearing delaminations. Additionally, the evaluation of the acquired images depends not only on the acquisition order, but also on the data of both cameras, as here the correlation between these images (taken at the same time) are also performed. As a result the correlation quality of a 3D-DIC system is better than that of a 2D-DIC system.

During quasi-static loading up to the measuring load $F_{da} = 15$ kN, images are captured every 500 ms until the measuring load is reached. Once this load is reached, the mode of the 3D-DIC is changed and images are captured every 500 cycles at the peak load. Furthermore, during the first 20k cycles, images are captured every 100 cycles so that the moment of damage initiation can be determined more accurately. After completing a cyclic loading sequence, the 3D-DIC measurement is terminated and manually restarted for the next sequence. The subset size needed for the assessment is selected in such a form that the overall error of correlation is 1%. The associated step size is picked with a quarter of the subset size. In Table 2, the parameters used for the 3D-DIC measurements are listed.

Table 2 Measurement parameters of the 3D-DIC system

Parameter	Dimension	Notes
Focal length	35 mm	identical for both cameras
Camera resolution	5 Mpx	
Camera distance	580 mm	distance to plate
	300 mm	distance between cameras
Subset size	29 px	
	1.556 mm	
Step size	7 px	
	0.3756 mm	

Active Thermography (AT)

Due to cyclic loading, structural components suffer damage, which might be below the surface and grow there without being observable from outside. One method to assess this is to use thermography. There are active and passive techniques, whereby active thermography is performed by using an external excitation, like a pulse excitation. If an external excitation is performed and there is damage, conduction of heat is reduced with respect to the undamaged area. This effect can be detected with a thermal imager and provides information of the damage [27, 28]. In contrast, the heat for passive thermography is caused only by the loading of the structural component itself. Passive thermography results are more diffuse and according to Paipetis et al. [29] passive thermography is only recommended when the temperature of the structural component is above the environmental temperature.

Consequently, active thermography with pulsed excitation is used in the performed experimental tests. The external lamp, which provides a constant illumination for the 3D-DIC, is deactivated for the duration of the measurements using active thermography, so that the influence of this heat source is suppressed. The measurements are carried out with the parameters indicated in Table 3.

Ultrasonic Flaw Detection (UFD)

Another method to assess damage is ultrasonic flaw detection [30]. Ultrasonic waves are emitted into the structural component by a transducer and received using either the reflection method or the transmission method. In the reflection method, the transducer also acts as receiver, whereas in the transition method, a separate receiver is required. The amplitude and the time it takes for the sound wave to propagate from the transducer to the receiver is monitored and provides information about possible defects. Various types of transducers are available to cover a wide range of applications. One type is the phased array transducer, with which several measurements can be carried out simultaneously. The phased array transducer is operated in reflection

Table 3 Measurement parameters of the AT measurement

Parameter	Dimension	Notes
Focal length	18.7 mm	
Camera resolution	382×288 px	
Frame rate	10 Hz	
Observation time	5 s	
Camera distance	210 mm	distance from lens to plate
Discretization	2×2 px	
	0.3 mm	

Table 4 Measurement parameters of the UFD measurement

Parameter	Dimension	Notes
Mode of measurement		pulse-echo
Speed of sound	3000 ms^{-1}	
Time resolution C-Scan	2.5 ns	
Gain	10 dB	
Pulse width	100 ns	
Radiation angle transducer	270°	
Aperture I	−0.09 mm	start
	0.2 mm	width
	4%	height
Aperture A	0.7 mm	start
	0.45 mm	width
	35%	height
Aperture B	0.46 mm	start
	0.57 mm	width
	7%	height
Scan resolution	1 mm	horizontal direction
	0.2 mm	vertical direction

method. However, it is necessary to couple the transducer to the structural components. In most cases, water is used. Thus, UFD belongs to the contact-based NDT methods. During the experimental tests, a phased array transducer (5L64-NW1), consisting of 64 elements of 1 mm width, in combination with a positioning encoder (ENC1−2.5-LM) is used to measure the size of the damage. With the positioning encoder, a two-dimensional measurement can be carried out, by merging single measurements of the individual positions. The incremental resolution of the position encoder is set to 0.2 mm. All measurements with UFD are carried out with the same settings. These are given in Table 4.

Data Evaluation - Processing of the Results

Images captured using the thermal imaging camera are processed in Matlab. The temperature increase caused by the heat input is obtained from two thermal images taken right before and after the thermal excitation. In this way, interfering heat is removed and only the heat that is decelerated by damage is visible. The acquired delta images are visualized within a temperature range from 0 to +1.3 °C.

The measurements carried out by UFD are visualized in C-Scan format. For this purpose, the visualizations are extracted straight from the Omniscan MX2 without additional processing. Using the identical settings and the same procedure, a changed result can be caused only by damage.

The 3D-DIC images of the first tested plate are used to determine an appropriate threshold value of sigma by matching the area of damage with measurements taken by AT and UFD. Therefore each individual quasi-static loading ramp is analyzed separately and the evaluated data are compared to the corresponding measurements of AT and UFD. In each case, the first image acquired in the quasi-static loading is used as reference image and subsequent images are evaluated on it.

The area of interest, on which the 3D-DIC evaluation is based, is defined surrounding the hole. In Fig. 5, the first image of a tested plate is shown. Additionally, the area of interest and the subset grid is depicted. Both, the area

of interest and the parameters of the 3D-DIC system are not modified. The evaluation of the individual quasi-static loading ramps of the first tested plate indicates that sigma = 0.01 is a suitable selection for the threshold value. The same threshold value is also used to assess damage initiation and damage propagation during cyclic loading, where the 3D-DIC images at peak load are used. In the 3D-DIC evaluation, the first image that is captured at peak load is considered to be the reference image. Meaning that the first image is at 70% peak load. Subsequent images at peak load
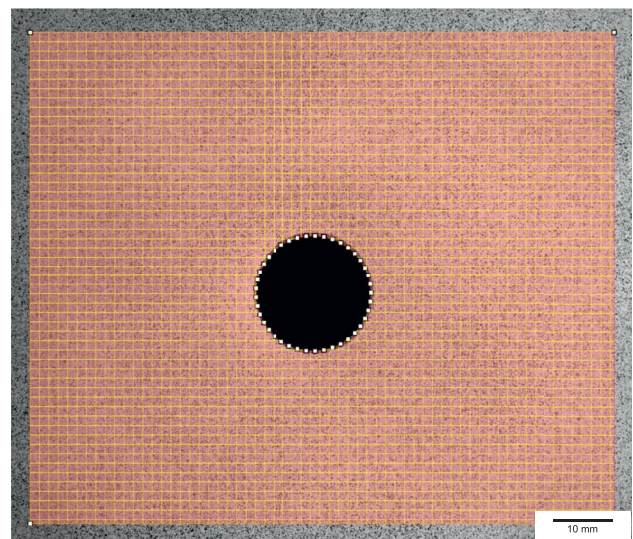
Fig. 5 Area of interest, consisting of subsets, of the first image taken with the 3D-DIC

are compared to the reference image and the changes due to damage are identified by using 3D-DIC sigma. To verify that the selected threshold value is also suitable for the other plates, a validation is performed, since sigma is obtained on the first tested plate. Again, the area of damage obtained with 3D-DIC sigma is compared to that of the corresponding AT and UFD measurements.

After 3D-DIC evaluation, post-processing of the data is performed in Matlab. Therefore the 3D-DIC evaluated data are spatially sampled at 0.25 mm intervals and an output for Matlab is generated. This gives a separate dataset for each evaluated image. A summation of all data points at which sigma exceeds the defined threshold value together with a multiplication of the interval area is carried out and gives the area of damage, without specifying the damage mode.

The number of cycles at which the images are acquired are also included. With this procedure, the damage propagation of the individual plates can be assessed.

Experimental Results

Based on the procedure defined in "Experimental Procedure" section, the experimental tests are executed. The results, and their validation, are presented in this section.

Initiation and Propagation of Damage

All plates are initially cycled for 20k cycles at 70% ultimate load. Within these 20k cycles, each plate experiences damage initiation. The number of cycles at which damage initiation occurs is determined as the first time sigma (3D-DIC result) passes the defined threshold value. Table 5 lists the number of cycles at damage initiation of the individual plates. Additionally, the area of damage at 20k cycles is listed.

Once 20k cycles are completed, the loading is increased to the test load level for damage propagation monitoring. The damage propagation of each plate is depicted in Fig. 6. On the vertical axis the area of damage and on the horizontal axis the corresponding number of cycles is plotted. The first 20k cycles are not included, since they are classified as part of the damage initiation. The damage size at 20k cycles is treated as an offset and subtracted from the paths of the individual plates. Missing data points are from pictures, which are excluded due to quality issues.

All plates were loaded by 2000k cycles. The tested load levels are reflected in the individual damage propagation paths, i.e. propagation is more significant at higher loads. This is manifested by a faster propagation at the beginning as well as by the final area of damage itself. Also, jump-like propagation appears more often and stronger, at higher load levels. For the plates tested at 70% ultimate load after 500k cycles, no significant further increase in the area of

Table 5 Number of cycles at damage initiation and area of damage after 20k cycles at 70% loading using sigma = 0.01

Plate number	Cycles until damage initiation according to 3D-DIC sigma	Area of damage at 20k cycles in mm²
1	1100	1.69
2	1300	1.05
3	1300	1.75
4	1000	2.44
5	900	2.75
6	900	1.94
7	1500	3.06
8	2500	2.10
9	1000	0.69
Mean value	1278	1.94
Variance	502	0.76

damage is observed. A similar behavior is obtained for the plates, which are tested at 80% ultimate load. During the first 750k cycles, jump-like propagation is observed, after which the area of damage approaches a constant value. The jumps appear for each plate at a varying cycle count. Also, the gain of damage caused by a jump varies. Nevertheless, all plates tested at the same load level finally developed a comparable size of the area of damage. The plate loaded with 90% of the theoretical ultimate load reveal a similar damage propagation to that of the plates tested at 70% and 80%. However, the damage grows faster and reaches a higher saturation level. The propagation of damage is most pronounced in plates tested at 100% ultimate load and advances throughout the whole duration of cyclic loading. To the end of the test,
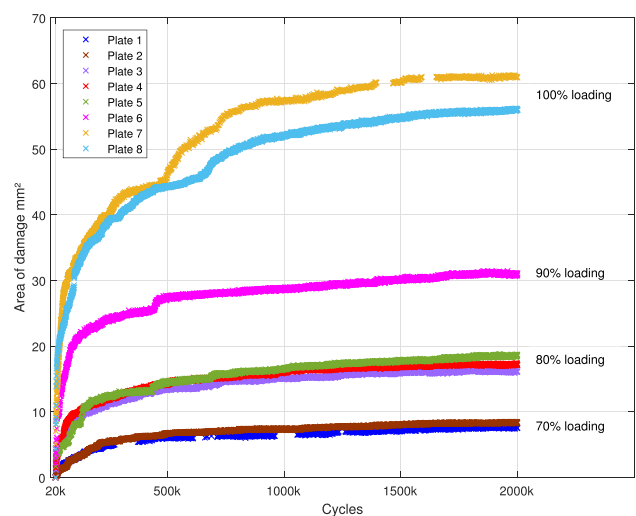
Fig. 6 Damage propagation of the individual plates obtained from 3D-DIC sigma

the propagation of damage tends to slow down. As before, jump-like propagation can be observed. The plate tested at 110% ultimate load failed in the first cycle. Consequently, this plate is not represented in Fig. 6.

Regardless of the selected test load level, a saturating behavior in terms of the area of damage is observed.

Validation

To ensure that the selected threshold value of sigma reflects the correct area of damage for all tested plates, a validation is required. For this purpose, the area of damage obtained with 3D-DIC sigma is compared to UFD measurements (C-Scan) and images taken with AT, at various numbers of cycles. In Fig. 7 exemplary comparisons for selected plates at chosen cycles are given. Since the measurements using AT and UFD are made on the back surface, these measurements are mirrored for a better comparison. The distortion of the hole at UFD measurements can be explained by the fact that the measurements are carried out by hand on the upright plate without being able to use a linear guidance. So the distortion is a result of a not perfectly straight movement during UFD measurement. Moreover, the different scan resolution (Table 4) also has an effect on the distortion.

For all performed measurements, a comparison of the area of damage determined with NDT methods (AT, UFD) with the area of damage obtained through 3D-DIC sigma agrees well. Thus the selected threshold value of sigma = 0.01 provides an acceptable value to assess the initiation and propagation of damage for all plates.
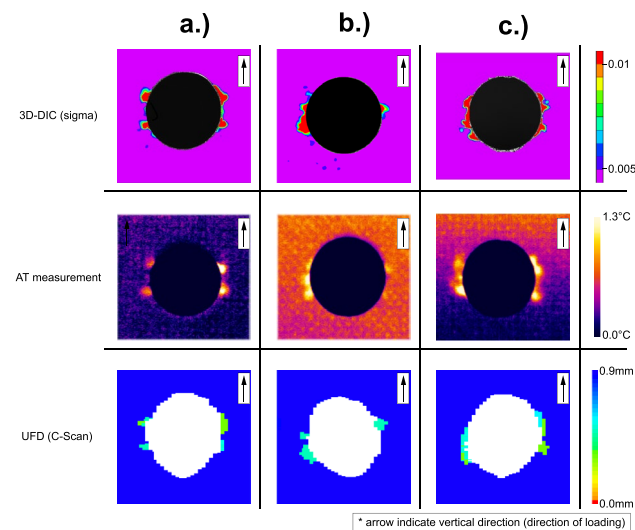
Fig. 7 Validation of the 3D-DIC threshold value by comparing the area of damage to AT and UFD (C-Scan) for, (**a**) plate 2 at 1750k cycles, (**b**) plate 3 at 2000k cycles and (**c**) plate 8 at 50k cycles

Empirical Model to Describe Damage Propagation

Based on the paths shown in Fig. 6, a model is developed that provides a good estimate of the propagation of damage for the individual plates. Therefore, a functional dependence between the area of damage A and the number of cycles N is specified. As indicated in advance, all tested plates reveal a saturating behavior in terms of the area of damage. To consider this within the model, the axis entries are swapped and an asymptotic term is inserted into the proposed model. In equation (1) the proposed model is presented. It includes three parameters C_0, C_1 and C_2, which are adjusted to fit the individual damage propagation paths of the individual plates. Initial propagation as well as subsequent slowing down of the propagation is determined using the parameters C_0 and C_1. The expression chosen in the denominator corresponds to the asymptotic term and ensures that the damage propagation reaches saturation. Consequently, the parameter C_2, indicates the asymptotic value for high number of cycles.

$$N(C_0, C_1, C_2) = \frac{C_0 \, A^{C_1}}{C_2 - A} \tag{1}$$

The proposed model is applied separately to each plate and the parameters C_0, C_1 and C_2 are determined. Each parameter is plotted versus the normalized nominal stress level x and a regression analysis for each parameter is performed. The normalized nominal stress level x is calculated by taking the ratio of the nominal stress (acting peak load/cross-sectional area) to the ultimate nominal stress (100% peak load/cross-sectional area). Consequently, the parameters C_0, C_1 and C_2 can be expressed as a function of the normalized nominal stress level x.

In Fig. 8 the least square fitting for the parameter C_0 is depicted. Additionally, the individual error bars (95% confidence interval) are shown. On the horizontal axis the normalized nominal stress level x and on the vertical axis the parameter C_0 is plotted. Both axes are presented in logarithmic form. A power function is selected to perform the regression, since it has the highest coefficient of determination R^2. Equation (2) shows the fitted function for the parameter C_0.

$$C_0(x) = 50 \, x^{-18.9} \tag{2}$$

The least square fit of parameter C_1 and the individual error bars (95% confidence interval) are given in Fig. 9. As before, the normalized nominal stress level x is plotted on the horizontal axis, while the parameter C_1 appears on the vertical axis. A linear relation between the parameter C_1 and the load level x is obtained, giving a high R^2 value. The associated function is given in equation (3).
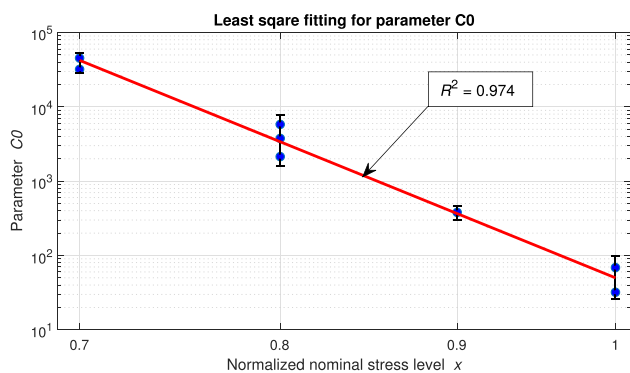
Fig. 8 Regression analysis for parameter C_0

$$C_1(x) = 3.14\,x \tag{3}$$

In Fig. 10 the regression of parameter C_2 is depicted. Also indicated are the individual error bars (95% confidence interval). On the horizontal axis, the normalized nominal stress level x is plotted. The parameter C_2 is plotted on the vertical axis. A clear exponential relationship between the parameter C_2 and the normalized nominal stress level x is apparent. This is reflected by a very high coefficient of determination. In equation (4) the associated function of C_2 is stated.

$$C_2(x) = 0.127\,e^{6.28\,x} \tag{4}$$

Equations (2) and (3) which express the individual parameters (C_0, C_1 and C_2) as a function of the normalized nominal stress level x, can be inserted into equation (1). This results in the expression given in equation (5).

$$N(x) = \frac{50}{x^{18.9}} \frac{A^{3.14\,x}}{0.127\,e^{6.28\,x} - A} \tag{5}$$

With this expression, the damage propagation under cyclic loading as a function of the normalized nominal stress level x can be described.

In Fig. 11, the measurements made with 3D-DIC are depicted in a similar way as in the Fig. 6. Only the measured
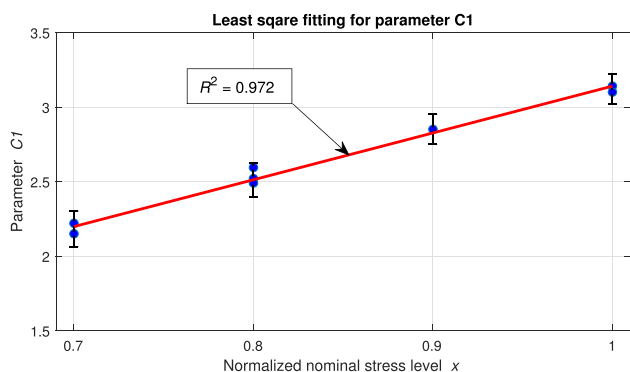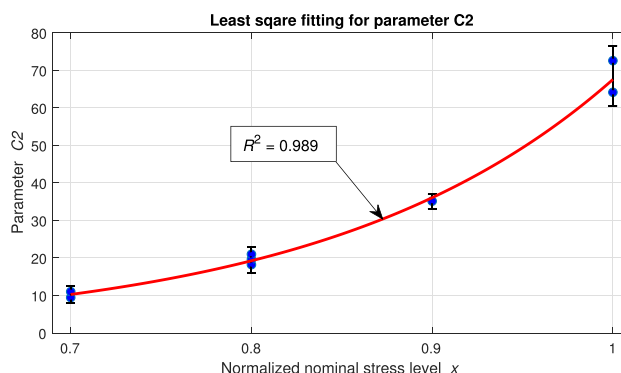

Fig. 9 Regression of the parameter C_1

Fig. 10 Regression of the parameter C_2

data points are reduced, so that only every twentieth entry is plotted. Moreover, the paths determined using the empirical model presented in equation (5) are included. The horizontal axis represents the number of cycles and the vertical axis the area of damage.

Discussion

Prior to the experimental testing, the individual plates were inspected for potential damages using UFD (C-Scan) and AT. There was no evidence of damage induced by water jet cutting at the edge of the hole, thus this manufacturing process did not affect the research content.

All plates were initially cycled at 70% ultimate load. This allowed the comparison of all plates in terms of damage initiation. In addition, this load level was selected to minimize any decrease in clamping force due to setting-in of clamping tabs. After 10k and 20k cycles, the clamping force was controlled and adjusted. It was found that setting-in of tabs was completed after 10k cycles and no further reduction occurred after that.

The additional measurements with UFD and AT made within the quasi-static loading were compared to the 3D-DIC evaluated data of the same loading. On the first
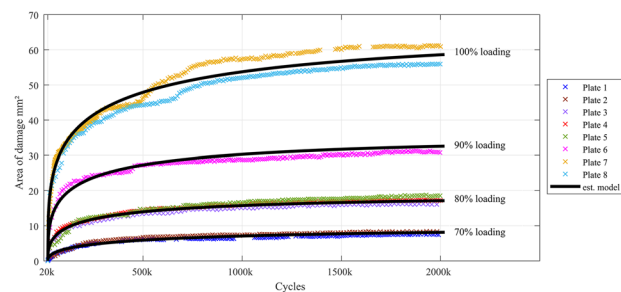

Fig. 11 Comparison of the empirical damage propagation model and the experimental evaluation by 3D-DIC

plate tested, these measurements were used to obtain a suitable threshold value for sigma, that adequately represents the area of damage. This was found by matching the area of damage expressed by 3D-DIC sigma with that from AT and UFD measurements. The same threshold value was taken for the other plates, but validated multiple times, as shown in Fig. 7. The validation of the threshold value for the other tested plates revealed that sigma $= 0.01$ was selected appropriately. During the selection of a suitable threshold value of sigma, evaluations with different threshold values were also carried out. This revealed that if the threshold value was selected in the range of 0.015 and 0.005, no differences in the results were apparent. Using a threshold value below 0.005, the noise of the correlation dominates, so that a clear assignment was not possible. A selection of sigma above 0.015, an assessment of the area of damage was no longer possible, as only very large changes to the plate could be detected. Regardless of the selection of the threshold value, the area of damage determined by AT and UFD (C-Scan) no longer agree with the area of damage obtained by 3D-DIC once sigma is selected beyond this range. Consequently, this strengthens the selection of sigma $= 0.01$ and indicates that sigma is not sensitive within this range.

The reference image for each plate was chosen to be the first image taken at peak load. In the context of strains, the reference image corresponds to the zero strain state, despite the fact that 70% of load is present. The offset has no influence on the selected quantity sigma, thus the choice of the reference image is correct. Due to the fact that 3D-DIC images were taken every 100 cycles, an accurate determination of the initiation of damage was possible.

The results of the individual plates are listed in Table 5. In all plates, damage initiation occurred after a short period of cycling. On average at 1278 cycles. Also the area of damage in all plates which was measured at the end of the damage initiation (20k cycles) showed a similar size of 1.94 mm^2.

In order to assess the damage propagation in CFRP specimens, the decrease in stiffness is frequently presented [31, 32]. For the considered plate with circular hole, the diameter of the hole is rather small with respect to the plate dimension, which means that there is no global change in stiffness or a global damage propagation. As shown by Broughton et al. [33] for glass fiber-reinforced plastic laminates, DIC can be used to localize sub-critical damage at the hole using the DIC calculated strains. A description of the damage size was not part of their investigation.

In contrast, based on 3D-DIC sigma, a damage size could be identified, which was used to establish an empirical model. This established empirical model provides a way to describe the damage propagation using the area of damage.

After 20k cycles, the load was adjusted to the test load level and damage propagation was assessed. The test load levels, which are given in Table 1, were chosen between 70%

and 110%. Following the findings of Aymerich and Found [9], and Ambu et al. [10], the load for the plate was chosen above the static failure load, to examine if the existing damage is large enough to handle this load. Therefore, plate 9 was tested at 110% ultimate load level, but suffered total failure in the first cycle. The total failure could be attributed to two potential causes. On the one hand, plate 9 has the smallest area of damage post damage initiation, meaning that the stress concentration has not degraded. One the other hand, the chosen load could have been too high. The other plates were tested for 2000k cycles and damage propagation was detected. As illustrated in Fig. 6, the test load level affects the damage propagation. The higher the selected test load level, the more pronounced the damage propagation. The fact that there is a sudden transition between static failure and very high fatigue life of the plate can be explained by this damage propagation. The size of the damage may be responsible for a change in the initial stress state at the hole, which yields a largely increased fatigue life.

The measurements performed with AT and UFD did not provide a precise physical classification of the damage mode. Here, further investigations using radiographic methods are required. Nevertheless, the area of damage contains each damage mode and allow the assessment of damage. Furthermore, cyclic creep and cyclic softening are included in the area of damage assessed with 3D-DIC sigma.

The damage initiation in plates with a circular hole at cyclic tensile loading was found to takes place at the hole. Further cyclic loading yields in damage propagation which grows from the hole into the plate. The damage propagation direction is normal to the loading direction. As matrix-dominated damage modes are also involved, delaminations can also propagate. Such delaminations, when debonding the plies, change the stress state around the hole and cause a change that was detectable with the 3D-DIC. Assuming the isolation of plies redistributes stresses from matrix to the fibres, an explanation for the increased fatigue strength is obtained. Arguably, such a damage may increase the static strength also, and will be scope of future research.

The paths of damage propagation shown in Fig. 6 were used to establish the empirical model with which the damage propagation in plates with a circular hole could be described. This empirical model was introduced in " Empirical Model to Describe Damage Propagation" section. The occurring jumps in the damage propagation are not considered in the established model. This is argued by the fact that plates which have been tested under the same load revealed that jumps are random and that a systematic relation could be ruled out. For each parameter, of the empirical model a functional relation with the normalized nominal stress level x was found and expressed. The parameter C_0, which describes the initial damage propagation, was approximated by a power function, which is given in equation (2). Swapping

the axis entries, necessary for the saturating behavior, is also reflected in the parameter C_0. As mentioned before, higher loadings cause stronger propagation at the beginning, thus the parameter C_0 is decreased at higher load levels and vice versa. The parameter C_1, which affects the initial propagation, as well as the propagation towards saturation behavior, exhibited a linear relationship with the normalized nominal stress level. Within the established model, the most interesting parameter is C_2, which represents the asymptotic value of damage for high cycles. For parameter C_2, an exponential relation associated with the normalized nominal stress level was identified. In equation (5), the established model with which the damage propagation in plates with an open hole could be described, with the parameters expressed by the normalized nominal stress level x was presented. The physical constraints were also covered by the empirical model. Provided that no load is applied, also no cycles are required to reach the appropriate area of damage. Also, if there is no area of damage, no cycles may be experienced so far.

In Fig. 11, the empirical model was compared with the 3D-DIC evaluated data. For the plates tested at 70% and 80%, the agreement appears to be better than for the plates tested at 90% and 100%. This is attributed to smaller pronounced jump-like damage propagation.

In the empirical model, only one hole size and plate geometry, along with only one load ratio and lay-up was tested, therefore the empirical model as a function of normalized nominal stress level was established only.

However, there will also be a functional relation to the hole diameter and hole location.

The established empirical model may also describe the propagation of damage if a different hole diameter is tested. For larger hole diameters, the applicability of the empirical model becomes restricted only if there is an interaction between the hole and the free edges, as damage propagation is mutually influenced here. This was observed by Nixon-Pearson et al. [32], aware that specimens with small dimensions were analyzed there. For smaller hole diameters, it is assumed that the damage propagation is similar to that of the considered hole. As the diameter of the hole becomes smaller, detection by 3D-DIC gets more challenging. As a consequence, there will also be a lower boundary to the empirical model in terms of the hole diameter. At the present stage, this limit is not known.

The influence of the hole location on the empirical model may be seen in a similar way. As far as the hole is not located to close to the edges, it is assumed that the empirical model could be used. If not, the free edges could interact with the hole [32], which is not reflected in the established empirical model.

There is also a large influence of the layup on the damage propagation and consequently on the established empirical model. To emphasize this, a comparison to already published research on holed CFRP specimens is done. Maciel

et al. [31] found that longitudinal splitting predominates the damage propagation in 5 Harness Satin $[0]_{8,s}$ laminates. Likewise, Ambu et al. [10] had investigated various cross ply laminates in their research. The X-radiographs presented there revealed that for the tested $[0/90]_{3s}$ laminates longitudinal splitting were primarily present. Contrary they showed, that for $[\pm 45/0/90]_{2s}$ laminates, delaminations between ± 45 and 0 plies at the hole had formed. The contour of the damage outlined therein shows a similarity to the area of damage determined with 3D-DIC sigma, as described in the present study. Although, their investigation showed significant matrix cracks that were provoked by the cross ply laminates. This leads to the conclusion that, the established empirical model can be used for other layup and laminates as well, assuming that plies of different orientations are stacked and that thin laminates are involved. The restriction to thin laminates can be attributed to the 3D-DIC method, as only changes on the surface and those that cause a change to the surface can be detected.

Overall it is assumed that the same general empirical model will hold. Nevertheless it depends strongly on the before mentioned variables, as well as on the laminate content, plate geometry and shape of the cut-out. However, further experimental research is required with different influencing variables in order to strengthen the assumption, that the established empirical model is valid. In summary, the presented empirical model can be used to assess the damage propagation of quasi-isotropic thin plain-woven CFRP plates with a circular hole exposed to cyclic tensile-tensile loading.

Conclusion

In this study the fatigue and progressive damage of thin plain-woven CFRP plates weakened by a circular hole was experimentally investigated. Under cyclic tension-tension loading the initiation and propagation of damage was assessed by 3D-DIC. For this purpose, the correlation goodness value sigma of the 3D-DIC was used to identify and quantify damage. The selected damage evaluation method, applying a threshold value to the sigma of 3D-DIC results was validated using AT and UFD. Based on the validated threshold value, the area of damage of the individual plates was determined over cyclic loading. The damage propagation of the individual plates revealed a similar systematic. Initially, the area of damage grew noticeably, followed by a slowing down of the damage propagation. The jump-like propagation of damage could be attributed to the CFRP plate, by matching the area of damage obtained from 3D-DIC with the measurements using AT and UFD. The load level is also represented in the final area of damage, the area of damage is larger at higher loads than at lower loads. Taking the area of damage as a basis, an empirical

model was developed with which the propagation of damage as a function of the selected load level could be derived. Comparing the established model and the measured data demonstrates good agreement. Since damage propagation can be well described with the established model, future work will include other hole sizes, different laminates and different stress concentrations (e.g. V-notch). Moreover, the influence of different ply orientations and load ratios will be part of further investigations to adapt the established model and make it more general.

Declarations

References

1. Strouhal M (2020) Corsia - carbon offsetting and reduction scheme for international aviation. Magazine of Aviation Development 8:23–28. https://doi.org/10.14311/mad.2020.01.03
2. Kisska-Schulze K (2012) Projections for reducing aircraft emissions. J Air Law Commer 77(4):701–746
3. Niu MCY (1999) Airframe structural design: practical design information and data on aircraft structures, 2nd edn. Hong Kong Conmilit Press Ltd., Virginia
4. Marsh G (2010) Airbus a350 XWB update. Reinf Plast 54:20–24. https://doi.org/10.1016/S0034-3617(10)70212-5
5. Lekhnitskii SG, Tsai SW, Cheron T (1968) Anisotropic Plates. Gordon and Breach Science Publishers, New York
6. Savin GN (1970) Stress distribution around holes. National Aeronautics and Space Administration – NASA TT F-607, Washington, D.C
7. Whitney JM, Nuismer RJ (1974) Stress fracture criteria for laminated composites containing stress concentrations. J Compos Mater 8:253–265. https://doi.org/10.1016/S0034-3617(10)70212-5
8. Karlak RF (1978) Hole effects in a related series of symmetrical laminates. Proceedings of Failure Modes in Composites III, American Society of Metals, 1977
9. Aymerich F, Found MS (2000) Response of notched carbon/peek and carbon/epoxy laminates subjected to tension fatigue loading. Fatigue Fract Eng Mater Struct 23:675–683. https://doi.org/10.1046/j.1460-2695.2000.00262.x
10. Ambu R, Aymerich F, Bertolino F (2005) Investigation of the effect of damage on the strength of notched composite laminates by digital image correlation. J Strain Anal Eng Des 40:451–461. https://doi.org/10.1243/030932405X16106
11. D7615 AS (2019) Standard practice for open-hole fatigue response of polymer matrix composite laminates. ASTM-D7615/D7615M-19, 1977
12. Sudarsono S, Ogi K (2017) Fatigue behavior of open-holed CFRP laminates with initially cut fibers. Open J Compos Mater 7:49–62. https://doi.org/10.4236/ojcm.2017.71003
13. Yongbo Z, Huimin F, Zhihua W, Xiaobing M (2015) Open hole fatigue characteristic and probabilistic model for fatigue life prediction of CCF300/QY8911 and T300/QY8911 composite laminates. J Compos Mater 49:3205–3214. https://doi.org/10.1177/0021998314561068
14. Muc A, Chwal M, Romanowicz PAS (2018) Fatigue-damage evolution of notched composite multilayered structures under tensile loads. J Compos Sci 2. https://doi.org/10.3390/jcs2020027
15. Kersemans M, Verboven E, Segers J, Hedayatrasa S, Van Paepegem W (2018) Non-destructive testing of composites by ultrasound, local defect resonance and thermography. Proceedings - 18th International Conference on Experimental Mechanics 2. https://doi.org/10.3390/ICEM18-05464
16. de Sá Rodrigues F, Marques R, Tabrizi IE, Kefal A, Ali HQ, Yildiz M, Afzal S (2021) A new methodology for thermoelastic model identification in composite materials using digital image correlation. Opt Lasers Eng 146:106689. https://doi.org/10.1016/j.optlaseng.2021.106689
17. Nobile R, Panella FWAP, Saponaro A (2022) Full-field monitoring methods for damage analysis on aeronautical CFRP specimens under fatigue loads. IOP Conference Series Materials Science and Engineering 1214. https://doi.org/10.1088/1757-899X/1214/1/012008
18. Pirinu, A., Panella, FW (2021) Fatigue and damage analysis on aeronautical CFRP elements under tension and bending loads: two cases of study. Int J Fatigue 152. https://doi.org/10.1016/j.ijfatigue.2021.106403
19. Schuermann H (2005) Konstruieren Mit Faser-Kunststoff-Verbunden. Springer, Berlin, Heidelberg
20. Montesano BHJ, Fawaz Z (2017) Influence of drilling and abrasive water jet induced damage on the performance of carbon fabric/epoxy plates with holes. Compos Struct 163. https://doi.org/10.1016/j.compstruct.2016.12.007
21. Standard ASTM, D4762–18 (2018) Standard guide for testing polymer matrix composite materials. ASTM D 4762–18:1977
22. Navarro P, Rogani A, Marguet S, Ferrero J-F (2021) Study of post-impact behaviour of thin carbon/epoxy laminates subject to fatigue tensile loading. Int J Fatigue 148. https://doi.org/10.1016/j.ijfatigue.2020.106134
23. Sutton M, Orteu J-J, Schreier H (2009) Image correlation for shape, motion and deformation measurements. Basic Concepts, Theory and Applications. Springer, New York
24. Solutions C (2019) Correlated Solutions – VIC-3D v8 reference manual
25. Sieberer S, Nonn S, Schagerl M (2020) Experimental study on the stiffness evolution and residual strength of a pre-damaged structural component made from SMC CFRP material. Proceedings of the 13th International Conference on Damage Assessment of Structures 148. https://doi.org/10.1007/978-981-13-8331-1-65
26. Sieberer S, Nonn S, Schagerl M (2019) Fatigue behaviour of discontinuous carbon-fibre reinforced specimens and structural parts. Int J Fatigue 131. https://doi.org/10.1016/j.ijfatigue.2019.105289
27. Maierhofer C, Myrach P, Reischel M, Steinfurth H, Röllig M, Kunert M (2014) Characterizing damage in CFRP structures using flash thermography in reflection and transmission configurations. Compos B Eng 57. https://doi.org/10.1016/j.compositesb.2013.09.036

28. Avdelidis NP, Almond DP, Dobbinson A, Hawtin BC, Ibarra-Castanedo C, Maldague X (2004) Aircraft composites assessment by means of transient thermal NDT. Prog Aerosp Sci 40. https://doi.org/10.1016/j.paerosci.2004.03.001

29. Paipetis AS, Grammatikos SA, Kordatos EZ, Barkoula N-M, Matikas TE (2011) Innovative non-destructive evaluation and damage characterisation of composite aerostructures using thermography. Plast, Rubber Compos 40. https://doi.org/10.1179/1743289810Y.0000000013

30. Scarponi C, Briotti G (1997) Ultrasonic detection of delaminations on composite materials. J Reinf Plast Compos 16. https://doi.org/10.1177/073168449701600901

31. Maciel MMAD, Shiino MY, Voorwald HJC (2020) Residual modulus degradation model for woven fabric composite determined by impulse excitation technique. Int J Fatigue 133. https://doi.org/10.1016/j.ijfatigue.2019.105456

32. Nixon-Pearson OJ, Hallett SR, Withers PJ, Rouse J (2013) Damage development in open-hole composite specimens in fatigue. Part 1: Experimental investigation. Compos Struct 106. https://doi.org/10.1016/j.compstruct.2013.05.033

33. Broughton WR, Gower MRL, Lodeiro MJ, Pilkington GD, Shaw RM (2011) An experimental assessment of open-hole tension-tension fatigue behaviour of a GFRP laminate. Compos A Appl Sci Manuf 42. https://doi.org/10.1016/j.compositesa.2011.05.014

Publisher's Note Springer Nature remains neutral with regard to jurisdictional claims in published maps and institutional affiliations.